PNAS RESEARCH ARTICLE | BIOPHYSICS AND COMPUTATIONAL BIOLOGY OPEN ACCESS

B56δ long-disordered arms form a dynamic PP2A regulation interface coupled with global allostery and Jordan's syndrome mutations

Cheng-Guo Wu[a,b], Vijaya K. Balakrishnan[a], Ronald A. Merrill[c], Pankaj S. Parihar[a], Kirill Konovolov[d], Yu-Chia Chen[a,e], Zhen Xu[f], Hui Wei[g], Ramya Sundaresan[a], Qiang Cui[h], Brian E. Wadzinski[i], Mark R. Swingle[j], Alla Musiyenko[j], Wendy K. Chung[k], Richard E. Honkanen[j], Aussie Suzuki[a,b,e], Xuhui Huang[b,d], Stefan Strack[c,1], and Yongna Xing[a,b,1]

Edited by Hao Wu, Harvard Medical School, Boston, MA; received July 1, 2023; accepted November 27, 2023

Intrinsically disordered regions (IDR) and short linear motifs (SLiMs) play pivotal roles in the intricate signaling networks governed by phosphatases and kinases. B56δ (encoded by *PPP2R5D*) is a regulatory subunit of protein phosphatase 2A (PP2A) with long IDRs that harbor a substrate-mimicking SLiM and multiple phosphorylation sites. De novo missense mutations in *PPP2R5D* cause intellectual disabilities (ID), macrocephaly, Parkinsonism, and a broad range of neurological symptoms. Our single-particle cryo-EM structures of the PP2A-B56δ holoenzyme reveal that the long, disordered arms at the B56δ termini fold against each other and the holoenzyme core. This architecture suppresses both the phosphatase active site and the substrate-binding protein groove, thereby stabilizing the enzyme in a closed latent form with dual autoinhibition. The resulting interface spans over 190 Å and harbors unfavorable contacts, activation phosphorylation sites, and nearly all residues with ID-associated mutations. Our studies suggest that this dynamic interface is coupled to an allosteric network responsive to phosphorylation and altered globally by mutations. Furthermore, we found that ID mutations increase the holoenzyme activity and perturb the phosphorylation rates, and the severe variants significantly increase the mitotic duration and error rates compared to the normal variant.

phosphatase | Jordan's syndrome | cryogenic electron microscopy

Significance

Intrinsically disordered regions (IDRs) and short linear motifs (SLiMs) are emerging key elements in complex signaling networks. The B56δ regulatory subunit of PP2A possesses long disordered arms with a substrate-mimicking SLiM. Here, we determined the cryo-EM structures of the PP2A-B56δ holoenzyme, revealing a super-long dynamic interface between these arms and the holoenzyme core that spans over 190 Å. This interface is closely coupled to the holoenzyme allosteric network and 20 disease-associated mutations, and phosphorylation of the arms is expected to perturb this interface. This study sheds light on the molecular mechanisms of B56δ disease mutations and the emerging machinery that relies on IDRs and SLiMs to modulate complex cellular processes and signaling.

Protein phosphatase 2A (PP2A) is a major serine/threonine phosphatase in the PPP family consisting of diverse heterotrimeric holoenzymes that target many cellular phosphoproteins in mammalian cells (1–6). Each holoenzyme consists of a common core formed by the scaffolding A (encoded by *PPP2R1A* or *PPP2R1B*) and catalytic C (PP2Ac; *PPP2CA*/*PPP2CB*) subunits and a diverse regulatory subunit (B) from one of the four major families [B/B55/PR55 (*PPP2R2*), B′/B56/PR61 (*PPP2R5*), B″/PR72 (*PPP2R3*), and B‴/Striatin]. Whole exome/genome sequencing identified mutations in PP2A subunits in cancer and largely de novo mutations in neurological disorders (7–11). Both unique and recurrent mutations have been found in the common core of the B56 regulatory subunits. Up to 20 recurrent missense mutations in B56δ cause severe intellectual and developmental disorders (8, 9, 12, 13), collectively known as Jordan's syndrome, or *PPP2R5D* -related neurodevelopmental disorder. More recently, multiple missense variants in B56δ have been associated with early-onset Parkinsonism (14–16). The incidence of neurodevelopmental and neurodegenerative disorders associated with B56δ is estimated at 2.5 per 100,000 births; about 250,000 cases are estimated to be undiagnosed (8, 9, 12, 14–16). Moreover, according to meta-analysis by the Simons Foundation, PPP2R5D is a category 1 autism risk gene (https://www.sfari.org).

Recent studies indicate that PP2A holoenzymes from the B56 family recognize a signature short linear motif (SLiM), LxxIxE, in the disordered regions of substrates (17–19). Diverse SLiMs are found in intrinsically disordered regions that serve as docking interfaces for peptide-binding proteins and play crucial roles in modulating cellular signaling (20, 21). Several SLiMs have been uncovered for the PPP family phosphatases targeting different substrates (22–25). The B56-targeting LxxIxE SLiM binds to a protein groove in the conserved common core of B56 regulatory subunits (19, 26). Several thousands of B56 SLiM-containing proteins are predicted in the human proteome. Many of these are involved in broad cellular and physiological processes (17). B56 regulatory subunits play essential roles in neurodevelopment, brain functions, and tumor suppression, as reflected by their ability to control cell cycle (17, 18, 27–29), cytoskeleton dynamics (30), DNA damage responses (31, 32), CREB signaling (33), and c-Myc stability (34–38).

Author contributions: Q.C., R.E.H., A.S., X.H., S.S., and Y.X. designed research; C.-G.W., V.K.B., R.A.M., P.S.P., K.K., Y.-C.C., Z.X., H.W., R.S., M.R.S., A.M., X.H., A.S., S.S., and Y.X. performed research; B.E.W. and W.K.C., contributed new reagents/analytic tools; C.-G.W., V.K.B., R.A.M., P.S.P., K.K., Y.-C.C., Z.X., R.S., R.E.H., A.S., X.H., S.S., and Y.X. analyzed data; and C.-G.W. and Y.X. wrote the paper.

The authors declare no competing interest.

This article is a PNAS Direct Submission.

[1]To whom correspondence may be addressed. Email: stefan-strack@uiowa.edu or xing@oncology.wisc.edu.

This article contains supporting information online at https://www.pnas.org/lookup/suppl/doi:10.1073/pnas.2310727120/-/DCSupplemental.

Published December 27, 2023.

In addition to the common core, B56δ possesses long disordered regions at the N- and C-termini that harbor multiple phosphorylation sites (*SI Appendix*, Figs. S1 and S2). The PP2A-B56δ holoenzyme is known to be highly regulated by distinct cellular signaling pathways. Protein kinase A (PKA) phosphorylates B56δ and activates the holoenzyme, thereby regulating signaling molecules downstream of cyclic adenosine monophosphate (cAMP) (39–41). At the G2/M checkpoint, the DNA-responsive checkpoint kinase Chk1 phosphorylates B56δ and stimulates the holoenzyme activity (42). B56δ also plays a critical role in controlling mitotic exit (43). Moreover, the B56δ holoenzyme is phosphorylated by the ataxia-telangiectasia mutated (ATM) kinase upon DNA damage and regulates p53 function (44). Understanding the structure of the PP2A-B56δ holoenzyme and the mechanisms by which it is activated is essential for shedding light on its complex regulation and the pathological mechanisms of its disease mutations.

Here, we report the high-resolution cryo-EM structures of a PP2A-B56δ holoenzyme bearing the E197K disease mutation, with its closed form determined at 2.7 Å. In the closed form, the long N/C-extensions of B56δ make cross-arm interactions, converging on itself and the holoenzyme core. This creates an extended dynamic interface that suppresses substrate access to both the phosphatase active site and the substrate SLiM-binding groove. Many previously identified phosphorylation sites and nearly all residues reported as mutations in individuals with intellectual disabilities (ID) are located at or near this interface. We further demonstrated that ID mutations alter the activation phosphorylation rates in response to cAMP-induced activation of PKA. ID mutations also alter the basal level of SLiM-binding and affect cell cycle progression and mitotic defects during cell division that could help explain macrocephaly observed in humans. Our studies reveal a coherent allosteric network of the holoenzyme that is responsive to phosphorylation and altered globally by ID mutations.

Results

Overall Cryo-EM Structures of the PP2A-B56δ Holoenzyme. Structure determination of the PP2A-B56δ holoenzyme by single-particle cryo-EM turned out to be challenging. We explored the "spotiton" technology (45, 46) to capture the dynamic states of the holoenzyme on the grids. The spotiton grids "purified' a closed form of the holoenzyme by dissociating the majority of the holoenzyme particles (*SI Appendix*, Fig. S3*A*). Albeit this form represents a small fraction of total particles, it gave a 4-Å map with uniform density for the long disordered regions at the N/C-termini (*SI Appendix*, Fig. S3*B*). We further explored glutaraldehyde and EDC (ethyl carbodiimide) crosslinks and tested different detergents and EM grids to control ice thickness and particle behavior. Nonetheless, the cryo-EM data for the crosslinked holoenzyme did not give a solid class of the closed form. Next, we examined the holoenzyme bearing different ID mutations and revealed two major forms for the E197K variant of the holoenzyme without chemical crosslinks: a closed form with a map of 2.59 Å (57.1% of particles) and a loose form with a map of 3.13 Å (42.9% of particles) (*SI Appendix*, Fig. S4). The E197K closed form aligns very well with that of the WT from the spotiton grid, with an RMSD of 1.2 Å (*SI Appendix*, Fig. S5*A*). The E197K closed and loose forms have a similar holoenzyme core, with an RMSD of 0.34 Å in their overlay (*SI Appendix*, Fig. S5*B*). At the same condition, we also collected a dataset for the WT holoenzyme. A slightly lower ratio of the closed form could be obtained for the WT holoenzyme by 2D classification. The cryo-EM map, however, was the poorest among all, indicating that the closed form for the WT holoenzyme is more dynamic than the mutant variants. The crystal structure of the PP2A-B56γ1 holoenzyme (PDB code: 2NYL) (47, 48), which represents the common core for the B56 family (*SI Appendix*, Fig. S1), fits the map for the B56δ holoenzyme core quite well. Since the N/C-arms are invisible in the loose form, we next focused on the structure of the closed form of the holoenzyme. As detailed later, the E197K closed form provides a structural platform for understanding the allosteric network of the holoenzyme and how it might be modulated globally by phosphorylation and other ID mutations.

The building of the N/C-arms in the closed form was guided by XL-MS (crosslink mass spectrometry). Using zero-length EDC crosslink followed by multiple protease digestions and MS runs, two crosslinked residue pairs in the N/C-arms gave detection frequency comparable to or better than those in the holoenzyme core (*SI Appendix*, Fig. S6). The structure of the E197K closed form was refined at 2.7 Å (*SI Appendix*, Table S1 and Figs. S4 and S7). It reveals extensive cross-arm interactions between the disordered regions of the B56δ termini; they interact with the holoenzyme core along a long path that spans over 190 Å (Fig. 1). While the long, linear interface involving two remote disordered arms is intrinsically dynamic in nature, it also harbors a significant

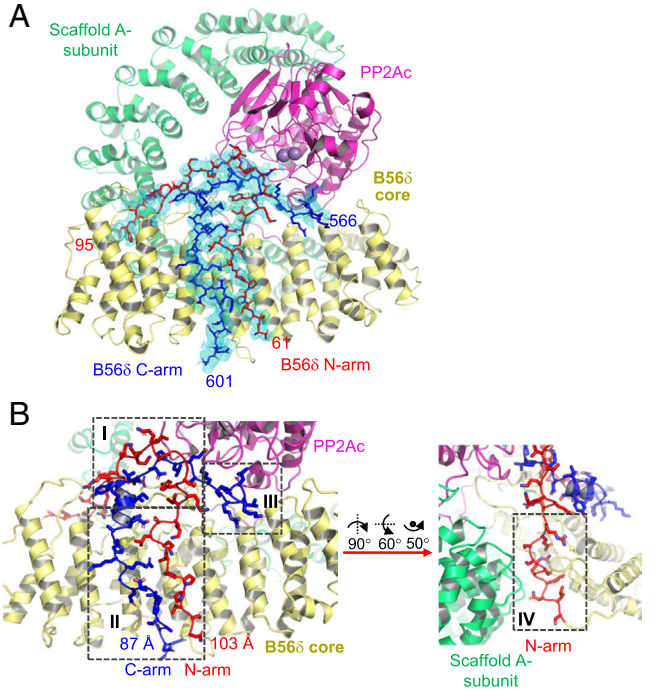

I: N/C-arm crossover-PP2Ac-B56-IL

	N/C	N-PP2Ac	C-PP2Ac	N-IL	C-IL
H-bonds	8	2	4	2	2
Hydrophobic	1	1			
salt bridge					1
unfavorable	1			2	2

II: N/C-arm-B56 core

	N/C	N-Core	C-Core-IL
H-bonds	3	4	8
Hydrophobic	5	2	5
salt bridge			
unfavorable			1

III: C-arm-PP2Ac-B56 core & IL

	C-PP2Ac	C-Core	C-IL
H-bonds		1	2
Hydrophobic	5	1	
salt bridge		1	1
unfavorable			

IV: N-arm-A-subunit-B56 core

	N-A	N-Core
H-bonds	3	8
Hydrophobic		3
salt bridge		1
unfavorable		2

Fig. 1. The cryo-EM structure of the closed form of the E197K PP2A-B56δ holoenzyme. (*A*) The overall cryo-EM structure of the E197K holoenzyme in the closed form. The A subunit, PP2Ac, B56δ core, and N/C-arms are colored green, magenta, yellow, red, and blue, respectively. The electron density map for N/C-arms is colored cyan. The N/C-arms are in sticks, and the rest of the structure is in cartoon. Manganese ions are shown in gray spheres. (*B*) Mapping of the contact properties along the path of the super-dynamic interface spanning over 190 Å. The presentation of the structural model and the color scheme are the same as in (*A*).

number of unfavorable contacts (Fig. 1*B*), underlying a long dynamic interface in this highly regulated holoenzyme.

The Extended Dynamic Interface in the PP2A-B56δ Holoenzyme. The above long-distance interface in the PP2A-B56δ holoenzyme centers at the N/C-arm crossover and makes close contacts with the PP2A catalytic subunit (PP2Ac) and the internal loop of B56 (B56-IL) (I) (Fig. 1*B* and *SI Appendix*, Fig. S8*A*). The N/C-arms are juxtaposed against each other toward the termini and make close contact with the B56δ core (II) (Fig. 1*B* and *SI Appendix*, Fig. S8*B*). Diverging from the crossover and perpendicular to the juxtaposed lower N/C-arms, the upper C-arm makes rich hydrophobic contacts with PP2Ac and miscellaneous contacts with the B56δ core and B56-IL (III) (Fig. 1*B* and *SI Appendix*, Fig. S8*C*); at the other side, the upper N-arm passes through the cleft between the A subunit and the B56δ core and makes different modes of contacts with both (IV) (Fig. 1*B* and *SI Appendix*, Fig. S8*D*).

Intriguingly, the N/C-arm crossover is most rich in repulsive contacts (Fig. 1*B*). Most prominently, E200 in B56-IL makes repulsive contacts to D578 in the C-arm and unfavorable contacts to several hydrophobic residues in the N/C-arms, I72, Y74, and I582 (Fig. 2*A*). In addition, E84 in the N-arm makes unfavorable contacts with Y580, a hydrophobic residue in the C-arm (Fig. 2*A*). These repulsive contacts, together with the energetically unfavorable bending of the N/C-arms, make the crossover the least energetically favorable structural elements along the extended dynamic interface. Other unfavorable contacts involve a nearby residue R86 in the upper N-arm (Fig. 2*A*). The E197K ID mutation creates two repulsive contacts to R571 and K73 in the C-arm and N-arm, respectively (Fig. 2*A*). Such changes might reduce the number of conformational states of the holoenzyme and thus allowed us to determine the structure of the closed form of the holoenzyme using single-particle cryo-EM.

We further mapped the hydrophobic contacts along the dynamic interface (Fig. 2*B*). While many small patches of hydrophobic contacts intertwine with the above unfavorable contacts, the dominant rich hydrophobic contacts are made by the two visible ends of the C-arm. L568 and L569 in the upper C-arm are nestled in a hydrophobic pocket formed by six PP2Ac residues and make close contacts with F416 from the B56δ core (Fig. 2 *B*, *Upper Right*). Near the C-arm's terminus, L595 interacts with I303 and H263 at the B56 SLiM-binding pocket, which is buttressed by contacts between F594 to P64/65/67 in the N-arm (Fig. 2 *B*, *Lower Right*). The distinct maps of energetically repulsive and favorable hydrophobic contacts likely dictate the complex regulation of the holoenzyme functions.

Dual Autoinhibition of the Holoenzyme and Roles of the N/C-Arms. The PP2A-B56 holoenzymes target specific substrates via the SLiM-binding pocket and the phosphatase active site that are around 30 Å apart (*SI Appendix*, Fig. S9). Phospho-substrates containing B56 SLiMs bind to the SLiM-binding pocket, which in turn places the nearby substrate phosphorylation sites close to the PP2A active site. The closed form of the holoenzyme establishes an elegant mechanism of dual autoinhibition, in which E574 and a cis-B56 SLiM (L_{595}TASQE$_{600}$) in the C-arm make close contacts to the PP2A active site and the B56 SLiM-binding groove (Fig. 3*A*). E574 in the C-arm mimics the substrate phosphate

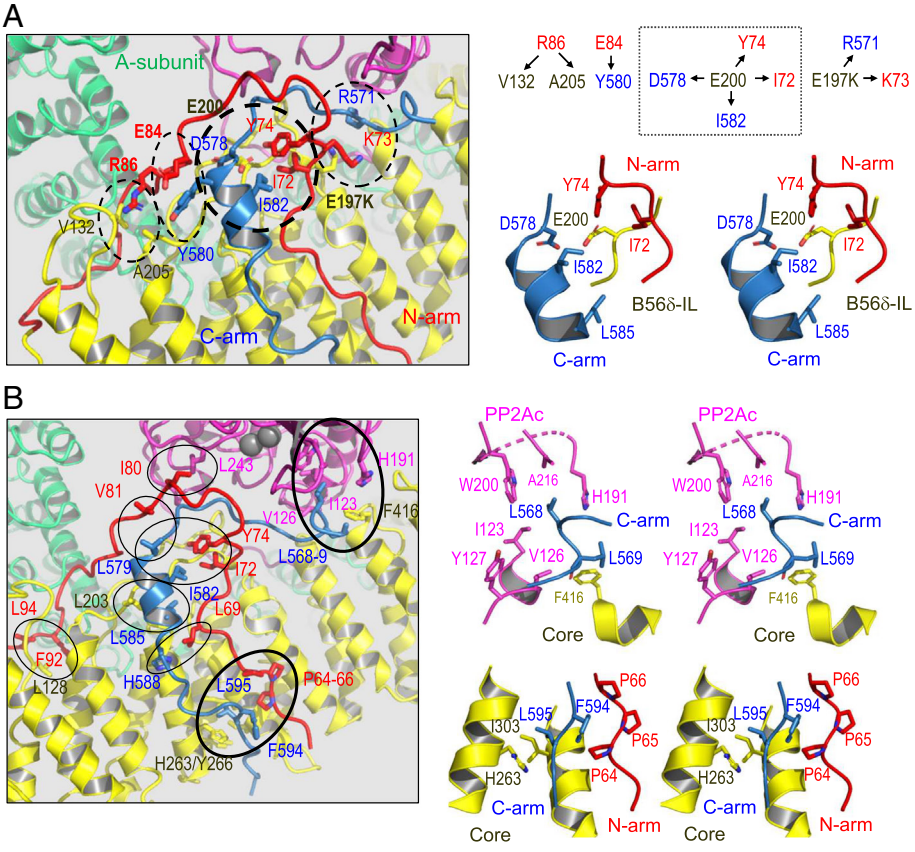

Fig. 2. Mapping and closeup views of unfavorable and hydrophobic contacts along the dynamic interface. (*A*) Distribution of unfavorable and repulsive contacts at the dynamic interface, highlighted in dashed cycles (*Left*) and illustrated at the upper right panel. The closeup stereoview of the central repulsive contacts with E200 is shown at the lower right panel. (*B*) Patches of hydrophobic contacts are in cycles and major hydrophobic interfaces are highlighted in thick cycles (*Left*). The closeup stereoviews for the latter are shown (*Right*). For (*A*) and (*B*), the color scheme is the same as in Fig. 1. The structural models are shown in cartoon and key residues at the interfaces in sticks.

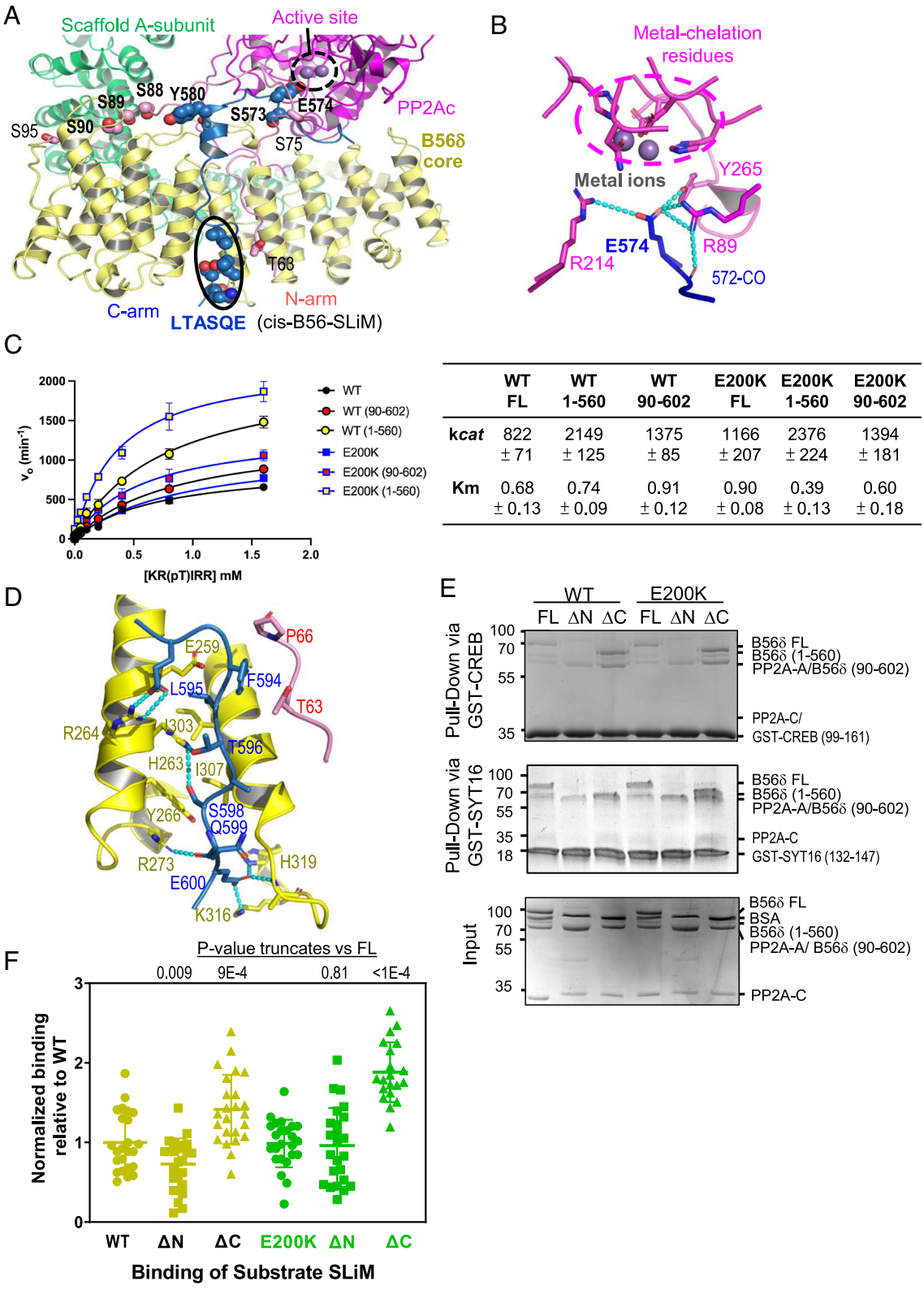

	WT FL	WT 1-560	WT 90-602	E200K FL	E200K 1-560	E200K 90-602
kcat	822 ± 71	2149 ± 125	1375 ± 85	1166 ± 207	2376 ± 224	1394 ± 181
Km	0.68 ± 0.13	0.74 ± 0.09	0.91 ± 0.12	0.90 ± 0.08	0.39 ± 0.13	0.60 ± 0.18

Fig. 3. Structural mechanism of dual auto-inhibition and roles of the B56δ N/C-arms. (*A*) The overall structure of the PP2A-B56δ holoenzyme highlights phosphorylation sites on the N/C-arms and residues essential for suppressing the phosphatase active site and the SLiM-binding groove. The structure is shown in cartoon and colored as in Fig. 1, except that the N/C-arms are colored pink and blue, respectively. Residues with key regulation functions and manganese ions (gray) are shown in spheres. (*B*) The closeup view of auto-inhibition at the phosphatase active site. The active site metal ions are in spheres. Active site residues and E574 from the C-arm are shown in sticks. (*C*) Truncations of either N- or C-arm increase the phosphatase activity of both the WT and E200K holoenzymes. (*D*) The closeup view of auto-inhibition at the B56 SLiM-binding groove, buttressed by extended interactions. (*E*) Examples of pulldown assays of the WT and E200K PP2A-B56δ holoenzyme full length (FL), truncation of N-arm (ΔN) or C-arm (ΔC) via GST-tagged CREB (99-161) (*Upper*) or GST-SYT16 (132-147) (*Middle*). One fifth of the holoenzyme input is shown (*Lower*). (*F*) All experimental repeats from (*E*) are normalized to the WT holoenzyme, and the scatter plots of the normalized results, averages of all repeats, and SD are shown. The *P*-values for the full-length versus truncated holoenzymes are calculated using Welch's *t* test. For (*B*) and (*D*), the structural models are shown in cartoon, and the color scheme is the same as in (*A*). Residues at the interfaces are shown in sticks. H-bond interactions are shown in cyan dashed lines.

and makes extensive H-bond and salt bridge interactions to basic residues at the PP2A active site (Fig. 3*B*). We hypothesize that autoinhibition of the holoenzyme is established by both N/C-arms. Consistent with this notion, deletion of the C-arm (1 to 560 or ΔC) in either the WT holoenzyme or the E200K disease variant drastically increases the phosphatase activity, and the truncation of the N-arm (90 to 602 or ΔN) also increases the phosphatase activity of both holoenzymes (Fig. 3*C*). While the binding of the cis-B56 SLiM to the SLiM-binding groove mimics the substrate SLiMs from substrates (19, 26), it is also buttressed by the hydrophobic contacts between the upstream F594 with the N-arm (Fig. 3*D*). Since the holoenzyme is rapidly denatured during isothermal titration calorimetry (ITC), most likely due to the super-dynamic nature of the N/C-arms, we assessed the binding of the GST-tagged substrate SLiMs from CREB (33) and SYT16 (17) to the full-length and truncated holoenzymes using pulldown assay (Fig. 3*E*). Due to the dynamic nature of the N/C-arms, multiple experiments with three batches of the holoenzymes were performed by multiple lab members to learn about the dynamic range of the substrate SLiM-binding (Fig. 3*F*). The calculated *P*-values showed significant differences between truncated and full-length holoenzymes. Intriguingly, while the truncation of the N-arm increases the phosphatase activity (Fig. 3*C*), it significantly decreases the binding of substrate SLiMs (Fig. 3 *E* and *F*). In contrast, truncation of the C-arm increases the binding of substrate SLiMs (Fig. 3 *E* and *F*). Our data suggested that the N/C arms confer coherent suppression at the phosphatase active site but opposing roles at the substrate SLiM-binding groove. It is likely that the kink on the C-arm stabilized by the N-arm is required for the suppression of the active site but causes structural tension toward the SLiM-binding groove (Fig. 3*A*). In the absence of the N-arm, the C-arm binds the SLiM-binding groove tighter with a relaxed kink. Its multipartite contacts with the holoenzyme core, particularly hydrophobic contacts, are largely intact (Fig. 2*A*).

Holoenzyme Responses to Phosphorylation of the Arms. In addition to the structural modalities for dual autoinhibition, the N/C-arms are rich in phosphorylation sites (Fig. 3*A*). Among these sites, S88, S89, S90, and S573 are the most frequently phosphorylated sites according to the PhosphositePlus database (https://www.phosphosite.org). S89, S90, and S573 make extensive H-bond interactions with acidic residues in the holoenzyme core, namely E95 from the scaffold A subunit, D130 in the B56δ core, and E198 in the B56-IL (Fig. 4*A*). Phosphorylation at all these sites is expected to create repulsive contacts that would disrupt the closed form and stimulate the loosening of the holoenzyme. Consistently, phosphorylation of mouse B56δ at S566 (corresponding to S573 of human B56δ) was found to be associated with the activation of the holoenzyme (40). Using an antibody that we developed to specifically recognize B56δ phosphorylation at S573 (*SI Appendix*, Fig. S10), we demonstrated a time-dependent increase of pS573 in vitro upon co-incubation of PKA and the holoenzyme (Fig. 4*B*) and in HEK293 cells upon forskolin-induced cAMP/PKA activation (Fig. 4*C*).

To detect the conformational changes associated with phosphorylation, we developed a split NanoBiT B56δ holoenzyme sensor, in which the SmBiT peptide fragment was inserted in the holoenzyme core immediately downstream of the N-arm and the LgBiT fragment was fused to the C terminus of the C-arm (*SI Appendix*, Fig. S11). The two NanoBiT fragments are spatially separated in the closed form. If the N/C-arms loosen upon activation phosphorylation by PKA, the two fragments can interact and form an active NanoBiT enzyme (*SI Appendix*, Fig. S11). By expressing the WT and E198K mutant holoenzymes bearing this holoenzyme conformation sensor in COS-1 cells, we showed that both holoenzymes produced increased NanoBiT luciferase activity in response to forskolin and rolipram, the combination of an adenine cyclase activator and a PDE4 inhibitor that increases intracellular cAMP levels (Fig. 4*D*). The responses of both WT and E198K were abolished by S573Q (Fig. 4*D*). Our structural and biochemical observations suggest that phosphorylation at S573 and possibly other sites on the arms might stimulate the loosening of the holoenzyme (Fig. 4*E*), which might facilitate the activation of the holoenzyme.

Effects of ID Mutations on the Holoenzyme Allosteric Network, Autoinhibition, and Phosphorylation. We reasoned that the super-dynamic interface in the PP2A-B56δ holoenzyme forms a coherent allosteric network connecting the phosphorylation sites and the structural elements for autoinhibition. Intriguingly, nearly all ID residues found in Jordan syndrome patients are spread throughout this dynamic interface (Fig. 5*A*). These mutations could allosterically impact the dissociation of the N/C arms to alter the holoenzyme activity. To gain critical insights into this allosteric network, we performed molecular dynamic (MD) simulations of the closed form of the holoenzymes for WT and two highly recurrent variants, E198K and E200K. Our initial 10 100-ns MD simulations were not successful in sampling the dissociations of the N/C arms. We thus adopted a recently developed enhanced-sampling technique: replica exchange with hybrid tempering (REHT) (49), which is a modified version of the popular replica exchange with solute tempering-2 (REST2) method (50) and has been shown to be particularly efficient for intrinsically disordered proteins. REHT is a rigorous enhanced-sampling technique which can reproduce the correct thermodynamic distributions at the 310 K, while allowing greater access to the conformational space by allowing a continuous MD simulation of the system to sample conformations at higher temperatures and with modified Hamiltonian. In our enhanced-sampling simulations, we included the terminal eight residues of the N/C-arms in a "hot region," and 20 replicas were run with the hot region temperatures spanning from 310 K to 600 K. These enhanced-sampling MD simulations resulted in a remarkable improvement in conformational sampling, which led to notable fluctuations in the tails and exposed the B56 SLiM-binding pocket, although a complete opening of the arms was not observed (*SI Appendix*, Fig. S12 *A* and *B*).

The conformations from the lowest temperature replica of the enhanced-sampling simulation were used to compute the allosteric network. The importance of a particular residue in the network was calculated as the number of shortest paths that cross the residue and normalized by the maximum. A residue was evaluated as important if its weight in the network was above a cutoff, defined as 80% of all residue weights in the network (*SI Appendix*, Fig. S12*C*, black dashed line in Fig. 5 *C* and *D*). Intriguingly, all ID residues in the B56δ core and phosphorylation sites on the arms are closely integrated into the allosteric network of the holoenzyme (Fig. 5*B*). Residues F473, I230, and L313 are located on the periphery, and their weight in the network is below the threshold. Either the E198K or the E200K ID mutation alters the residue weights of other ID residues and phosphorylation sites in the allosteric network (Fig. 5 *C* and *D*), suggesting that ID mutations globally perturb the coherent dual autoinhibition and phosphorylation-enhanced holoenzyme loosening.

Assessing the effects of ID mutations on the holoenzyme function, including substrate SLiM binding and activation phosphorylation rates, turned out to be very challenging. The reproducibility between experimental repeats is considerably low. Given the super-dynamic nature of the B56δ holoenzyme, we initiated an effort to critically control the purification procedures, aiming to

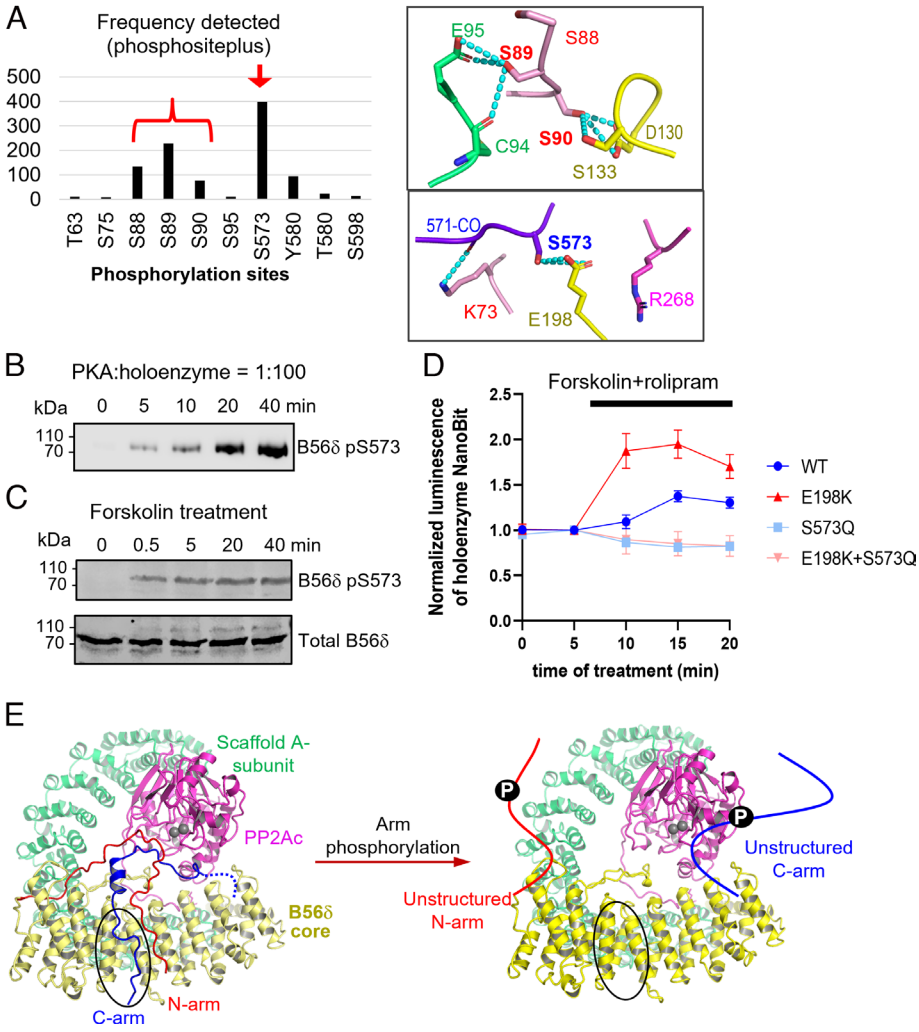

Fig. 4. Responses of the PP2A-B56δ holoenzyme to phosphorylation of the arms. (*A*) The most frequently detected phosphorylation sites on the N/C-arms are highlighted (as summarized from https://www.phosphosite.org) (*Left*). The closeup views of these serine residues on the N/C-arms and their interactions at the dynamic regulation interface (*Right*). The color scheme is the same as in Fig. 3*A*. Phosphorylation at these sites is expected to create repulsive contacts. (*B*) Time-dependent changes in pS573 of the PP2A-B56δ holoenzyme by PKA in vitro. (*C*) Time-dependent increase of B56δ pS573 upon cellular activation of cAMP/PKA. (*D*) Time-dependent conformational changes of the PP2A-B56δ holoenzyme (WT and E198K) in mammalian cells upon cellular activation of cAMP/PKA by forskolin and rolipram. The non-phosphorylatable mutation of B56δ, S573Q, abolishes this response. (*E*) The model of phosphorylation-induced loosening of the N/C-arms. The color scheme is the same as in Fig. 1.

precisely control the holoenzyme behavior. We tested two different strains of Hi5 host cells, varied the salt concentrations between 50 mM and 150 mM, and compared French press and Dounce in cell disruption. These variations did not lead to any improvement in the dynamic range of the data. No difference was observed in the basal level of holoenzyme phosphorylation. The super-dynamic nature of the holoenzymes was also reflected by the fact that the holoenzymes rapidly denatured and formed aggregates during ITC (isothermal titration calorimetry) experiments, suggesting that the holoenzyme might be hyper-sensitive to shearing force.

Nonetheless, summarizing the results from up to 10 batches of WT and mutant holoenzymes from the above effort, we observed a statistically significant increase in substrate SLiM binding by the E198K ID mutation despite the dynamic range of the data (Fig. 5*E*). E420K also shows a substantial effect on the basal substrate SLiM-binding; in contrast, the E200K and E197K variants gave mild effects (Fig. 5*E*). We further examined the effects of ID mutations on the holoenzyme conformation using a holoenzyme FRET (fluorescence resonance energy transfer) sensor. A tetracysteine peptide (TC) fused to the C terminus of the B56δ subunit was used to generate TC-FLASH, which serves as an acceptor for CFP fused to Pro53 at the N terminus. The WT B56δ-holoenzymes with this sensor exhibited a higher energy transfer efficiency compared to the E198K mutant, indicating E198K-B56δ subunit adopts a more relaxed conformation than WT (Fig. 5*F*), consistent with the increased basal substrate SLiM-binding of this disease variant (Fig. 5*E*). To better understand how the E198K mutation affects the shape of the holoenzyme in solution, we performed size exclusion chromatography, multi-angle light scattering, and small-angle X-ray scattering (SEC-MALS-SAXS) experiments. The E198K protein had a larger radius of gyration (Rg) and maximum dimension (Dmax) than the wild-type protein, as seen by the shift in the distribution of interatomic distances in the normalized Pair-distance function [P(r)] and the normalized Kratky plot. (Fig. 5*G* and *SI Appendix*, Fig. S13). This SAXS data analysis reveals E198K has a more elongated conformation compared to the wild type.

Next, we assessed time-dependent changes of pS573 upon forskolin-induced cAMP/PKA activation in WT and CRISPR-edited HEK 293 cells bearing homozygotic E198K, heterozygotic E200K, or homozygotic E420K (51). While the pS573 level of the WT holoenzyme is increased at a stable rate, the phosphorylation rate of the disease variants fluctuates in a large range among all experimental repeats (Fig. 5*H*). Our data support a notion that the tight coupling of the dynamic interface, the holoenzyme allosteric

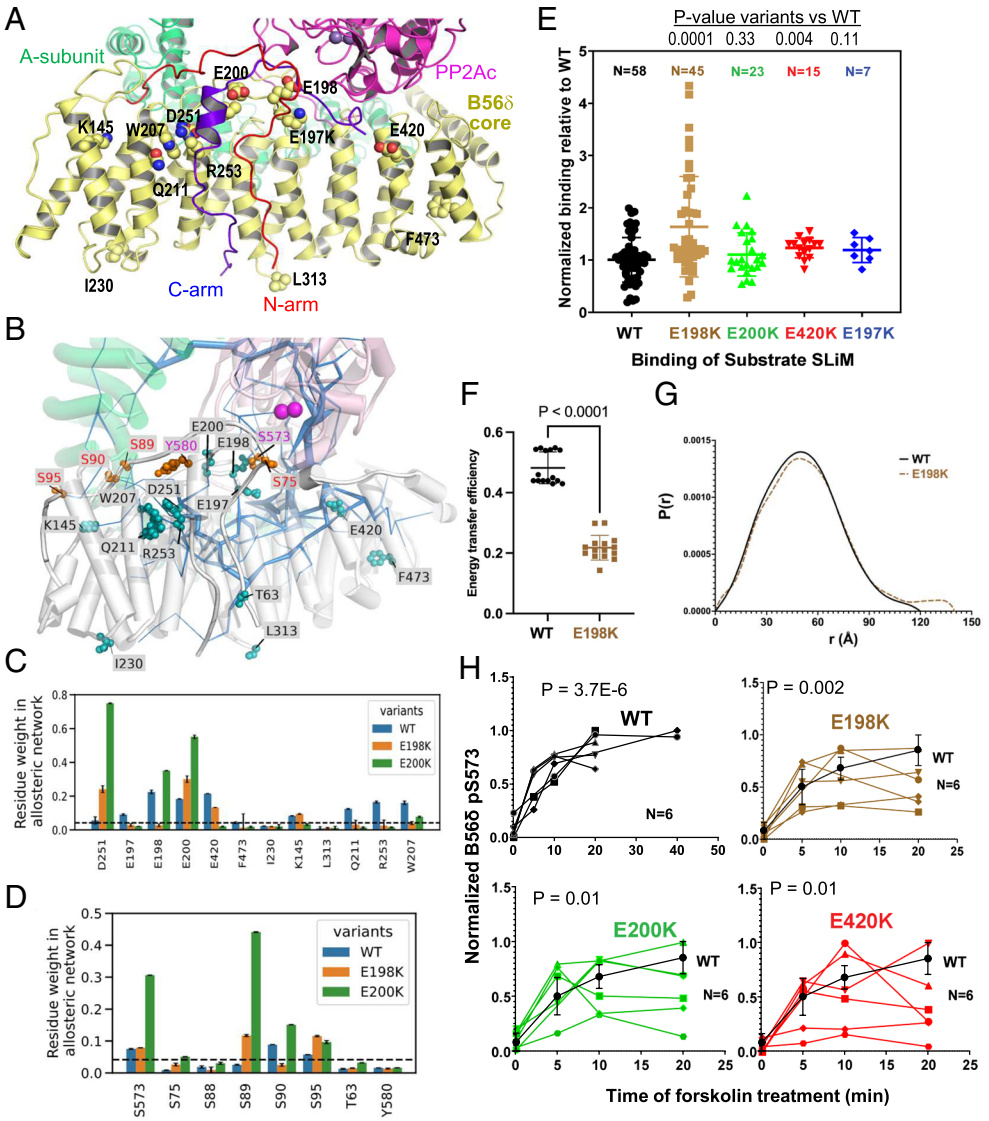

Fig. 5. The allosteric network of the PP2A-B56δ holoenzyme, perturbation by B56δ ID mutations, and effects on holoenzyme functions. (*A*) The overall structure of the B56δ holoenzyme highlights the B56δ ID residues predominantly located at the dynamic regulation interface. (*B*) Illustration of the allosteric network of the PP2A-B56δ holoenzyme and its relationship to ID residues (green ball-and-stick) and activation phosphorylation sites on N/C-arms (orange ball-and-stick). The allosteric weights are shown as the thickness of blue wires. They are estimated from the enhanced-sampling simulations of the WT holoenzyme, modified from the cryo-EM structure of the E197K holoenzyme in the closed form. (*C* and *D*) The global perturbation of residue weights of ID residues and activation phosphorylation sites on the allosteric network by E198K and E200K. The results in (*B–D*) are the average of 20 enhanced-sampling simulation trajectories. (*E*) Pulldown of WT and mutant holoenzymes by GST-tagged CREB (99-161) assessed the effects of ID mutations on substrate SLiM binding. The data is normalized with the binding intensity of WT. The number of repeats, their scatter plots, averages, and SD are shown. The *P* values for comparison of WT and disease variants are calculated using Welch's *t* test. (*F*) FRET assay measuring the distance (energy transferring efficiency) between the N terminus and C terminus of the B56δ subunit in WT and E198K PP2A-B56δ holoenzyme. Means ± SD are shown (N = 15). (*G*) The normalized Pair-distance function P(r) plot generated from SAXS analysis on the WT and E198K PP2A-B56δ holoenzymes. (*H*) Time-dependent phosphorylation of S573 in HEK293 cells expressing WT and mutant B56δ upon cellular cAMP/PKA stimulation. The experiments were repeated six times. Means ± SD was calculated for WT for comparison to disease variants. The *P*-values for time-dependent changes were calculated using the Jonckheere–Terpstra test.

network, the regulatory structural elements, and ID mutations renders the disease mutations to differentially modulate the basal activity and the activation phosphorylation rates of the holoenzyme. These highly intertwined structural and functional connections are expected to be highly sensitive to experimental conditions and cellular signaling contexts.

Effects of B56δ ID Mutations on Cellular Phosphatase Activity and Mitosis. To examine the effects of B56δ ID mutations on the phosphatase activity in vivo, a tandem of 11 B56 SLiMs, with a range of binding affinities to B56 and containing CDK-consensus phosphorylation sites, was fused to the N terminus of cyclin dependent kinase 5 (CDK5) (referred to as CDK5-B56 SLiM). Upon co-transfection into mammalian cells, auto-phosphorylated CDK5-SLiM (pCDK5-SLiM) serves as a substrate for the PP2A B56δ-holoenzyme (Fig. 6*A*). Dephosphorylation could be demonstrated upon the inhibition of CDK5 by dinaciclib. We compared the rate of dephosphorylation of the pCDK5-SLiM by the WT and E198K PP2A B56δ-holoenzymes and showed that E198K mutant dephosphorylated the SLiMs with a significantly increased rate compared to the WT (Fig. 6 *B–D*). The increased activity of E198K is consistent with the enhanced binding of B56 SLiM shown earlier (Fig. 5*E*). The result here demonstrated that B56δ ID mutations lead to abnormal PP2A activity toward its substrates in the cells.

B56 SLiMs are predicted in broad signaling proteins involved in different stages of the cell cycle (17). Building on previous

observations of the role of B56δ at the G2/M checkpoint (42) and mitotic exit (43), we examined whether the ID mutations E198K, E200K, or E420K (introduced by CRISPR editing) affect the mitotic duration and fidelity of HEK293 cells. We used high temporal resolution live-cell imaging to monitor the mitotic progression in HEK293 cells with either WT or mutant B56δ (*SI Appendix*, Fig. S14). The stages of mitosis were determined using a far-red SiR-DNA dye. In WT cells, the duration of mitosis, measured from nuclear envelope breakdown (NEBD) to anaphase onset, was 27 ± 6 min (n = 100). This duration was significantly longer in the E198K (33 ± 10 min, n = 100) and E420K (31 ± 10 min, n = 100) mutant cells (Fig. 6*E*). However, when treated with an MPS1 inhibitor to counteract the spindle assembly checkpoint (SAC) (52), the difference in mitotic duration between WT and mutants, like E420K, was eliminated. Both durations converged to a similar range: 22 ± 6 min for WT and 22 ± 7 min for

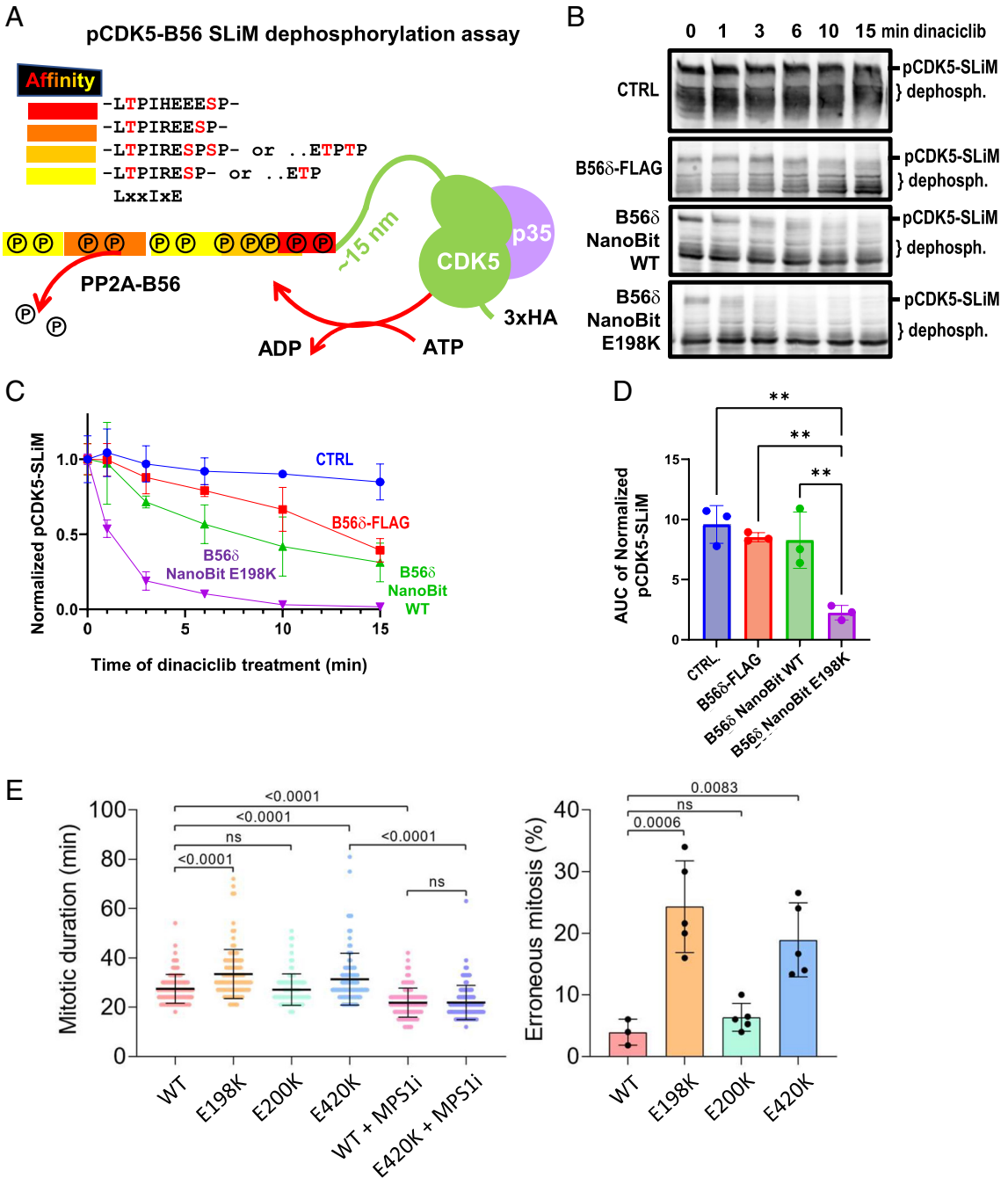

Fig. 6. Effects of B56δ ID mutations on cellular PP2A-B56δ activity, mitotic progression, and mitotic errors. (*A*) Illustration of the cellular PP2A-B56 activity assay. Phosphorylation-dependent B56 SLiMs in varied binding affinities (color coded) were fused to CDK5 and expressed from the same plasmid as the CDK5 activator p35. (*B*) Representative HA-immunoblot of HEK293T whole cell lysates expressing a control protein (CTRL, monomeric YE289RR-mutant B56δ), FLAG-tagged B56δ, or the B56δ-SmBiT/LgBiT conformation sensors (WT or E198K) after treatment with 2 μM of the CDK5 inhibitor dinaciclib for 0 to 15 min. Electrophoretic mobility of the CDK5-B56 SLiM substrate by SDS-PAGE ranges between ~55 and 75 kD and is influenced by cellular CDK5 and PP2A activity. (*C*) Densitometric quantification of the experiment in (*B*) (Means ± SD from duplicate blots). (*D*) Area-under-the-curve (AUC) quantification of dephosphorylation time courses (individual AUCs and Means ± SD from N = 3 independent transfections are plotted). (*E*) Mitotic durations from NEBD to anaphase onset (*Left*) and the frequency of mitotic errors (*Right*) in the cells shown in *SI Appendix*, Fig. S14 are plotted. Means ± SD was calculated and shown. The *P* values for comparison of WT and disease variants are calculated using the one-way ANOVA (*Left*) and two-tailed *t* test (Right).

E420K (Fig. 6*E*). This suggests that the prolonged mitosis in the mutants is SAC-dependent. Interestingly, E200K mutant cells displayed a mitotic duration comparable to WT (28 ± 4 min, n = 100) and significantly shorter than both E198K and E420K mutants. Consistent with these observations, both E198K and E420K cells, which represent the most severe disease variants, showed a significantly higher frequency of mitotic errors compared to WT or E200K cells (Fig. 6*E*). Mitotic errors are known to lead to inappropriate SAC activation and consequently prolonged mitosis (52, 53).

Discussion

Our cryo-EM structures of the PP2A-B56δ holoenzyme, particularly in its closed form, reveal distinct mechanisms by which it can exist in a dual-inhibition latent state that is responsive to phosphorylation. The extended dynamic regulation interface of the holoenzyme provides a coherent framework for understanding the holoenzyme's dual latency and activation, as well as the shared mechanisms underlying the diverse disease mutations associated with neurological disorders. The complexity of the holoenzyme regulation resides in the extended regulation interface primarily formed by the intrinsically disordered regions rich in regulatory elements. These elements include multiple phosphorylation sites on both N/C-arms, a cis-B56 SLiM and E574 on the C-arm, which establish dual autoinhibition in the closed form, and other signaling sequences on the C-arm, such as nuclear localization signal (NLS) and SH3-binding motif. In addition, the regulation interface is featured by multiple repulsive contacts that contribute to its semi-stable and dynamic nature, which is responsive to phosphorylation and disease mutations. Furthermore, our simulations reveal an allosteric network closely coupled to the regulation interface, reflecting the structural intricacy and coherency underlying complex holoenzyme regulation.

The mutation spectrum in patients also corroborates our above notions on the regulation interface in the B56δ holoenzyme. The latter, in turn, provides critical insights into the underlying mechanisms of ID-associated disease mutations. Albeit the mutated residues of diverse variants are widely separated spatially, the super-long regulation interface harbors nearly all of them like an extended umbrella. The coupling of ID mutations to the regulation interface and the allosteric network explains their shared symptoms, including intellectual disability, hypotonia, and autism (8, 9, 12, 13). ID mutations at the holoenzyme regulation interface might perturb the holoenzyme regulation and function in many scenarios, potentially leading to dominant negative effects. For example, ID mutations might perturb the dual latency individually or simultaneously and alter the phosphorylation rates of the holoenzyme. Furthermore, the loss of coherent dual latency and perturbed holoenzyme activation might also lead to untimed exposure of NLS and binding sites for SH3 and 14-3-3. Consistent with the latter notion, a family with B56δ missing the C-arm showed incomplete penetrance of neurological disorders compared to other missense variants that are de novo and completely penetrant (54). The effects of B56δ mutations are also supported by studies using CRISPR-edited HEK293 cells bearing heterozygotic or homozygotic E420K (51). This mutation in either single or both alleles perturbs the same diversity of signaling nodes.

The involvement of the B56 SLiM and its binding groove at the regulation interface likely contribute to the bulk of the broad range of clinical symptoms of Jordan syndrome. The human proteome has ~1,500 B56 SLiM-containing proteins involved in broad cellular signaling and processes (17). Perturbation of the dual latency and holoenzyme phosphorylation is expected to affect many of these B56 SLiM-containing signaling proteins. Intriguingly, the increased mitotic duration and error rates caused by E198K (Fig. 6*E*) correlate very well with the elevation of its B56 SLiM-binding in vitro (Fig. 5*E*) and SLiM-dependent phosphatase activity in cells (Fig. 6 *A*–*D*). Furthermore, CRISPR-edited HEK293 cells bearing B56δ E420K altered 6% of phosphopeptides in the proteome by at least twofold (51). We noticed that among ~1,000 genes in the SFARI Gene database with genes associated with autism and neurodevelopmental disorders (https://www.gene.sfari.org), >10% possess B56-targeting SLiMs, underlying overlapping molecular processes perturbed by Jordan's syndrome and other SFARI genes. In addition to the effects of ID mutations on mitosis (Fig. 6*E*), the E420K mutation was shown to affect mTOR/AKT signaling among other signaling processes (51). Coupling to PP2A holoenzyme SLiMs is an emerging theme of signaling and functional complexity. For example, the multiple PP2A holoenzyme SLiMs in the PP2A methylesterase (PME-1) creates versatile PME-1 activities toward PP2A holoenzymes, diverse signaling pathways, and cellular processes (31).

In addition to the shared mechanisms across variants, our study begins to illuminate the molecular basis of the genotype–phenotype correlation of clinical severity. Clinical studies showed that E198K is the most severe form of the disease and that E420K is more severe than the E200K and E197K variants (8, 9, 12). We showed that the E198K holoenzyme has a much higher basal level of substrate SLiM-binding than the WT holoenzyme and other disease variants (Fig. 5*E*). Furthermore, E198K and E420K cause longer mitotic duration than WT and E200K and gave higher mitotic error rates than the E200K variant (Fig. 6*E*). In a companion paper focusing on the changes of the holoenzyme allosteric paths by E198K and E200K, we showed that the E198K holoenzyme has an allosteric pathway resembling the phosphorylated holoenzyme, underlying a higher basal activity and reduced latency of this variant (55). In contrast, the allosteric pathway is minimally affected by E200K. Many questions remain to be answered. Our study laid the critical foundation for understanding the function and regulation of the B56δ holoenzyme and an in-depth understanding of the underlying mechanisms of Jordan syndrome mutations.

It is important to stress the super-dynamic nature of the regulation interface formed by the disordered N/C-arms and the holoenzyme core, which might be highly sensitive to shearing force as reflected by aggregation in ITC experiments and the dynamic range of B56 SLiM-binding (Fig. 5*E*). Our challenges to capture the closed form of the WT holoenzyme by single-particle cryo-EM suggest the presence of many conformation states that might be required for numerous nuances of cellular signaling under normal physiological conditions. Two distinct structural features might contribute to the super-dynamic nature: the interactions of two extended intrinsically disordered regions from the widely separated N/C-arms and the multiple unfavorable contacts along the interface. Enriching broad regulation elements in the disordered regions forms one more basis for the complexity and intricacy of this regulation interface. The structural and functional features outlined here might not be unique to the B56δ holoenzyme but are a common theme for modulating complex biological processes and signaling that remain to be broadly studied.

Materials and Methods

More details in *SI Appendix*.

Molecular Cloning and Protein Preparation. All protein constructs were generated by standard PCR molecular cloning strategy. The human His_6-tagged scaffold A subunit (α isoform), His_8-tagged PP2Ac (α isoform), and GST-tagged B56δ were overexpressed in insect cells using the lab-modified Bac-to-Bac

baculovirus expression system (56, 57). The point mutations for the B56δ disease variants and/or truncations of the B56δ N/C-arms were introduced by site-directed mutagenesis. WT and mutant holoenzymes were expressed and purified as described in *SI Appendix*. GST-tagged SYT16 (132–147) and CREB (99–161) were overexpressed in *Escherichia coli* DH5α and purified over GS4B resin and ion exchange chromatography.

GST-Mediated Pulldown Assay. To test the interaction between WT and mutant PP2A-B56δ holoenzyme with substrate B56 SLiM peptides, 12 μg of GST-tagged SYT16 (132–147) or GST-tagged CREB (99–161) immobilized on GS4B resin was incubated with 10 μM of PP2A-B56δ holoenzymes for 5 min. The proteins bound to the resin were examined by SDS-PAGE and visualized by Coomassie blue staining. Details are presented in *SI Appendix*.

Cryo-EM Sample Preparation and Data Acquisition. The cryo-EM grids for the WT PP2A-B56δ holoenzyme were prepared at the New York Structural Biology Center using a prototype of the commercial Chameleon system (SPT Labtech) based on the Spotiton technology (45, 46). Using a piezo-electric dispenser, 50 pl of the WT holoenzyme at a concentration of 1.6 mg mL^{-1} was applied to the homemade self-wicking nanowire grids (58), followed by plunge-frozen in liquid ethane. The robot chamber was operated at room temperature without strictly controlled but moderate humidity. The cryo-EM data for the WT holoenzyme were collected using the Titan Krios (ThermoFisher) electron microscope operated at 300 kV equipped with Gatan K2 summit cameras. A total of 1,790 movies were automatically acquired by Leginon (59) with a defocus range of −1.2 μm to −2 μm at a nominal magnification of 105,000×, corresponding to a pixel size of 1.096 Å/pixel. Each stack dose-fractioned over 50 frames was recorded with a total electron dose of 66.84 $eÅ^{-2}$.

For the E197K PP2A-B56δ holoenzyme, an aliquot of 3 μL of purified holoenzyme at 0.4 mg mL^{-1} was applied onto a glow-discharged holey gold grids (UltraAuFoil R1.2/1.3), blotted for 4 s with a blot force of −5 and plunge frozen in liquid ethane using a FEI Vitrobot Mark IV (Thermo Fisher Scientific) at 4 °C and 100% humidity. Cryo-EM data were collected using a Titan Krios operating at 300 kV with a Gatan K3 detector and GIF Quantum energy filter. A total of 9,158 movies were collected using SerialEM, with a slit width of 20 eV on the energy filter and a defocus range from −0.7 μm to −2.2 μm in super-resolution counting mode at a nominal magnification of 81,000×, corresponding to a pixel size of 1.068 Å/pixel. Each stack dose-fractioned 69 frames was recorded for a total exposure time of 3.2 s and electron dose of 49 $eÅ^{-2}$.

Cryo-EM Data Processing. All data were processed with similar strategies and procedures using cryoSPARC 3.0 (60). Movies were motion-corrected using Patch Motion Correction, followed by the contrast transfer function (CTF) estimation using Patch CTF Estimation. Images with bad CTF estimations worse than 4 Å were discarded. Particles were first picked from thirty good images using Blob Picker and extracted with a box size of 280 Å. Good 2D class averages showing projections in different orientations were selected as templates for automatic picking for the entire dataset. Reiterate 2D classification was used to remove bad particles. The remaining good particles were used for ab initio reconstruction, followed by heterogeneous and homogenous refinements, with particles from bad classes removed in each reiterate procedure. Different conformations of the PP2A-B56δ holoenzyme were best separated by 3D variability analysis (3DVA) (61). Particles from conformationally homogeneous classes were then subjected to homogenous refinement, followed by local and global CTF refinement. Local refinement with a mask around the closed conformation of the B56δ subunit was performed to obtain a better resolution for this subunit. These efforts gave maps with a resolution of 3.13 Å for the loose form and 2.59 Å for the closed form of the E197K PP2A-B56δ holoenzyme. The resolution was estimated by applying a soft mask around the protein complex and using the gold-standard Fourier shell correlation (FSC) = 0.143 criterion.

Model Building and Refinement. The initial model of the PP2A-B56δ complex was built on the structure of PP2A-B56γ1 holoenzyme (PDB ID: 2NPP) and manually docked into the cryo-EM maps in Chimera (62). Modifications to the holoenzyme core and model building of the N/C-arms were performed in COOT (63). The structural model was refined using the phenix.real_space_refine program in PHENIX (64) with secondary structure and geometry restraints. The final models were analyzed using MolProbity (65).

B56δ Holoenzyme Phosphorylation by Protein Kinase A (PKA) In Vitro and upon cAMP Activation in Cells. In vitro, 100 μL PP2A-B56δ holoenzyme was prepared to a final concentration at 0.1 mg mL^{-1} in assay buffer containing 50 mM Tris-HCl (pH 7.5), 10 mM $MgCl_2$, 200 μM ATP, 0.1 mM EDTA, 2 mM DDT, and 0.01% Brij35. Phosphorylation was initiated by adding 1 μL PKA at 0.1 mg mL^{-1} to the PP2A-B56δ holoenzymes [PKA: PP2A-B56δ = 1: 100 (w/w)] and incubating the mixture at 37 °C. Samples taken at the indicated time point were examined by western blot. To detect the phosphorylation level at S573 of B56δ, we developed and untilized an antibody that recognizes pS573 (*SI Appendix*). The total B56δ was detected by a commercial antibody (Invitrogen, MA-26636).

Human embryonic kidney (HEK293T) cells were cultured as described in *SI Appendix*. Following transit transfection of the Flag-tagged B56δ (WT, E198K, E200K, and E420K), the HEK293T cells were treated with 10 μM forskolin (Fsk; Sigma: 344270-10MG) and 1 mM isobutylmethyxanthine (IBMX; Cayman:13347) to stimulate cellular cAMP/PKA. The cells were harvested at the indicated time following stimulation and lysed in the presence of 10 μM H89 (PKA inhibitor) and phosphatase inhibitor (phoSTOP, Sigma-Millipore). The levels of pS573 were determined as above and normalized to the total B56δ. At least six experimental repeats were performed to determine the fluctuation range of the activation phosphorylation rates. The *P*-values for the time-dependent increase of pS573 were calculated using the Jonckheere–Terpstra test in MSTAT 7.0 (https://oncology.wisc.edu/mstat/).

Enhanced-Sampling Molecular Dynamics Simulations. The cryo-EM structure of the closed form of the E197K PP2A-B56δ holoenzyme was used to generate the initial model for the close forms of WT, E198K, and E200K holoenzymes. Molecular dynamics (MD) simulations were performed using Gromacs (66) patched with PLUMED 2.8.0 in the Amber ff14SB forcefield (67). The protonation state of protein residues was determined by propka 3.4.0. The short-range Coulomb interactions were cut off at 0.9 nm, and long-range electrostatics were computed with PME (particle–mesh Ewald). The Lennard-Jones interactions were cut off at 0.9 nm. The structure was simulated in a dodecahedron box, with a minimum distance to the surface of the protein of 1 nm. The complex was solvated in TIP3P water (approximately 60,000 water molecules), and sodium ions were added until the system was neutral. The energy of the system was minimized with the steepest descent algorithm for 10,000 steps. Then, 1 ns MD simulations were performed at 310 K with the positions of all protein atoms except hydrogen restrained. In these simulations, the temperature was controlled by a V-rescale thermostat with a coupling constant of 10 ps, and pressure set to 1 bar controlled by a C-rescale barostat with a coupling constant of 1 ps. Snapshots used for analysis were spaced by 100 ps.

Conventional MD simulations are not successful in sampling the dissociations of the N/C-arms. We thus have adopted a modified version of REST2 (50) enhanced-sampling technique: i.e., replica exchange with hybrid tempering or REHT (49). In particular, our enhanced sampling simulations consisted of 20 replicas of the system simulated in parallel, with exchanges between simulation conditions attempted at 1-ps intervals. This means that a copy of our system, which initially starts at 310 K can be exchanged to explore the dynamics at higher temperatures, allowing it to cross energy barriers rapidly. All the exchanges satisfy the detailed balance (i.e., only a fraction of exchange attempts are accepted based on the detailed balance condition), ensuring that the correct Boltzmann distributions are maintained at all temperatures. When analyzing the data, we only include the MD conformations sampled at the 310 K and with unmodified protein potential energy. By scaling its potential energy, REST2 only tempers the selected hot region of the protein but keeps the waters at 310 K, and the bath temperature is constant across all the replicas. In our simulations, we slightly modified the REST2 protocol and also raise the bath temperature mildly up to 324.3 K following the REHT protocol (49). The terminal 8 residues of the N/C-arms were placed in a hot region. Twenty independent replicas were run with the hot region calculated temperatures assigned to a geometric progression: 310, 320, 332, 344, 356, 368, 381, 395, 409, 423, 438, 454, 470, 486, 503, 521, 540, 559, 578, and 600 K. Exchanges between replicas were attempted every 500 steps and the acceptance probability achieved was ~20%. Our enhanced-sampling simulations were conducted up to 100 ns, totaling 2 μs of simulation time per PP2A variant. The allosteric networks were computed as detailed in *SI Appendix*.

Mammalian Cell Holoenzyme Sensor to Detect Conformation Changes in Response to cAMP Activation. N-terminal large (LgBit) and C-terminal small (SmBit) fragments derived from NanoLuc (Promega) were fused to the C terminus of B56δ and inserted downstream of its N-arm at residue 103, respectively. The SmBit sequence is sandwiched by a short linker sequence, "GSG" at both ends to alleviate structural hindrance for complementation with LgBit. The constructs expressing the B56δ holoenzyme conformation sensors were transfected into COS-1 cells. After 24 h, cells were placed in 20% Nano-Glo® Live Cell Reagent (Promega) mixed with 80% DMEM containing 1% FBS. Cells were equilibrated at 37 °C in 5% CO_2 in a Cytation 5 before the luminescence readings were measured every 5 min. Following the second reading, cells were treated with 20 μM forskolin (Tocris) and 2 μM rolipram (Tocris) to activate adenylyl cyclase and inhibit cAMP phosphodiesterase 4 (PDE4) simultaneously to activate cellular cAMP/PKA. All values were normalized to the vehicle control, and all wells were normalized to the 5-min time point (just before forskolin/rolipram treatment). The experiments were performed in quadruplicate and repeated three times. Representative results were shown. Error bars represent SD.

FRET Assay. FRET assay was performed as described previously with minor modifications (31). 0.5 μM purified PP2A-B56δ holoenzyme containing CFP-B56δ (53-602)-TC fusion protein were measured with excitation at 450 nm and emission at 490 nm in the presence (1:1.5 molar ratio = protein: compound) or absence of FLAsH-EDT2 (Invitrogen, T34561) using ClarioStar Plate Reader (BMG LABTECH). FLAsH-EDT2 compound was conjugated to CFP-B56 (53-602)-TC to generate the TC-FLASH fluorophore, which acts as an acceptor in the FRET assay. The rate of energy transfer was calculated based on the loss of donor (CFP) fluorescence using the following equation: E = 1−(FDA/FD), where FDA and FD are the fluorescence of CFP in the presence and absence of TC-FLAsH, respectively.

Size Exclusion Chromatography Coupled with Multi-Angle Light Scattering and Small-Angle X-ray Scattering (SEC-MALS-SAXS) and Data Processing. SEC-MALS-SAXS data sets were collected using the 18-ID-D BioCAT Beamline at the Advanced Proton Source (APS) at Argonne National Laboratory (Chicago, IL). Samples were centrifuged for 5 min at 13,000 rpm to remove any potential aggregates prior to column loading. Samples containing 1.5 mg mL^{-1} of WT or mutant PP2A-B56δ holoenzymes in 550 μL were injected onto a 24 mL Superdex 200 10/300 GL column (GE Healthcare) equilibrated with 25 mM Tris pH 8.0, 150 mM NaCl, and 50 μM $MnCl_2$ at a flow rate of 0.7 mL min^{-1} on an Agilent 1300 chromatography system. Column eluant was analyzed in line by the UV absorbance detector of the Agilent 1300 chromatography system, then subsequently directed into the DAWN Heleos-II light scattering (LS) and OptiLab T-rEX refractive index detectors in series. Finally, the elution trajectory directed samples into a 1.0-mm ID quartz capillary SAXS sample cell. Scattering data were collected every 1 s using a 0.5-s exposure and detected with a Pilatus 3 1 M pixel detector (DECTRIS) with a 12 KeV (1.033 Å wavelength) X-ray beam covering a q-range of $0.004 < q < 0.356$ Å^{-1} ($q = 4\pi/\lambda \sin\theta$, where λ is the wavelength and 2θ is the scattering angle). Accurate protein molecular weights from MALS data were determined using the ASTRA 7 software (Wyatt Technology). SAXS data reduction was performed automatically using custom scripts to generate radially averaged scattering curves of normalized intensity versus q value. For each protein, the buffer scattering before and after the eluted peak were recorded and used for background correction.

Following data reduction, buffer subtraction, SAXS data were further analyzed using BioXTAS RAW version 2.1.1 (68). Protein peaks were also run-through evolving factor analysis (EFA) to deconvolute peaks into the individual scattering components where applicable. The forward scattering intensity I (0) and radius of gyration (Rg) were calculated from the Guinier fit. The normalized Kratky plot, pair distance distribution plot, or P(r), and Porod volume (Vp) were calculated using the program GNOM embedded in BioXTAS RAW software.

In Vivo Phosphatase Assay Using the CDK5-B56 SLiM Fusion Substrate. The CDK5-B56 SLiM fusion protein was generated, and its phosphorylation states were determined as described in the *SI Appendix*. Phosphorylation of CDK5-B56 SLiM is reversibly controlled by cellular PP2A-B56 and CDK5-p35 and reaches the highest level when the tethered CDK5 is active. The PP2A-B56 activity is assessed by measuring the rate of dephosphorylation upon inhibition of CDK5. Briefly, HEK293T cells were seeded at ~200,000 cells per well in 24-plates for same day transfection using Lipofectamine-2000 as described (69). Plasmids expressing Flag-tagged B56δ or B56δ-NanoBit and CDK5-B56 SLiM protein were transfected at 2:1 (w/w) ratios. After 16 to 24 h, serum-containing media was replaced by OptiMEM and dephosphorylation was initiated by addition of the selective CDK5 inhibitor dinaciclib (2 mM) to wells. Reactions were stopped by freezing plates in liquid N_2 and lysing cells in SDS sample buffer. Whole cell lysates were separated by SDS page, immunoblotted for the HA tag, and scanned with a LiCOR Odyssey scanner. The increase in electrophoretic mobility of the CDK5-B56 SLiM fusion protein was quantified by densitometry using a custom-written macro for ImageJ that is available (from S.S.) upon request.

Live Cell Imaging and Mitotic Duration Measurements. To investigate whether the B56δ ID mutation, E198K, E200K, or E420K affects the mitotic duration and fidelity, we used high temporal resolution live-cell imaging to monitor the mitotic progression of HEK293T cells with the WT B56δ or CRISPR knock-in ID mutation. A Nikon Ti-2 inverted microscope equipped with a Hamamatsu Fusion camera, spectra-X LED light source (Lumencor), Shiraito PureBox (TokaiHit), and a Plan Apo 20× objective (NA = 0.75) controlled by Nikon Element software was used for live imaging. Time-lapse imaging collected three frame 3D stacks at 2 μm steps along the *Z* axis at 3 min intervals for 24 h. All cells were grown on a four-chambered glass bottom dish (#1.5 glass, Cellvis) in FluoroBrite DMEM media (Thermo Fisher) supplemented 10% FBS (Gibco) and 2 mM GlutaMAX (Gibco). All cells were incubated with 250 nM sirDNA (Cytoskeleton, Inc.) for 3 h before live imaging. Cells were recorded at 37 °C with 5% CO_2 in a stage-top incubator using the feedback control to maintain the growing media's temperature (Tokai Hit, STX model). Image analysis was performed using Nikon Element software. Mitotic stages were determined by nuclear staining. The mitotic duration was measured from nuclear envelope breakdown (NEBD) to anaphase onset. Incidences of lagging chromosomes, unaligned chromosomes, and chromosome bridges were analyzed. The experiments were independently repeated two times for mitotic duration measurements (total of n = 100) and three to five times for error measurements (n = 50 in each replicate). *P*-values between variants were calculated by the one-way ANOVA and two-tailed *t* test. *P*-values <0.05 were considered significant.

Data, Materials, and Software Availability. The electron microscopy maps of the loose and closed form of E197K PP2A-B56δ holoenzyme have been deposited in the Electron Microscopy Data Bank with accession codes EMD-42018 (70) and EMD-41837 (71), and the atomic models have been deposited in the Protein Data Bank with accession codes 8U89 (72) and 8U1X (73). The small-angel scattering data of WT and E198K PP2A-B56δ holoenzyme have been deposited in Small Angle Scattering Biological Data Bank with accession codes SASDTW2 (74) and SASDTX2 (75).

ACKNOWLEDGMENTS. We thank Drs. Derek Taylor and Wei Huang from Case Western Reserve University for discussions on cryo-EM grid freezing, Drs. Bridget Carragher and Clint Potter from NYSBC (New York Structural Biology Center, currently Chan Zuckerberg Imaging Institute), and Dr. Janette Myers from PNCC (Pacific Northwest Cryo-EM Center) for assistance and discussions on cryo-EM data collection, and Kenneth Satyshur and Ivan Andrewjeski from School of Medicine for IT support. Cryo-EM data collection was supported by Simons Foundation at NYSBC and NIH grant U24GM129547, performed at PNCC at OHSU, and accessed through EMSL (grid.436923.9), a DOE Office of Science User Facility sponsored by the Office of Biological and Environmental Research. SAXS study used resources of the Advanced Photon Source, a U.S. Department of Energy (DOE) Office of Science User Facility operated for the DOE Office of Science by Argonne National Laboratory under Contract No. DE-AC02-06CH11357. This project was supported by NIGMS 9 P41 GM103622. This study is supported by NIGMS R01 GM137090-01 (Y.X.), R01 GM 145811 (Y.X.), Jordan's Guardian Angels Foundation, and Jordan's syndrome research consortium fund from the State of California SB840 and SB129 #44 (Y.X., sub-awards A19-3376-S007 and A22-2853-S007; S.S., sub-awards A19-3376-S004 and A22-2853-S004; PD/PI: Nolta, Jan), NIGMS R35 GM147525 (A.S.), the Simons Foundation Autism Research Initiative (#877875, S.S.), and the Hirschfelder Professorship Fund (X.H.).

Author affiliations: [a]McArdle Laboratory for Cancer Research, Department of Oncology, University of Wisconsin at Madison, School of Medicine and Public Health, Madison, WI 53705; [b]Biophysics Program, University of Wisconsin at Madison, Madison, WI 53706; [c]Department of Neuroscience and Pharmacology, University of Iowa, Iowa City, IA 52242; [d]Chemistry Department, University of Wisconsin at Madison, Madison, WI 53706; [e]Molecular and Cellular Pharmacology Program, University of Wisconsin at Madison, Madison, WI 53706; [f]Protein and Crystallography Facility, University of Iowa, Iowa City, IA 52242; [g]The Simons Electron Microscopy Center, New York Structural Biology Center, New York, NY 10027; [h]Department of Chemistry, Boston University, Boston, MA 02215; [i]Department of Pharmacology, Vanderbilt University, Nashville, TN 37232; [j]Department of Biochemistry and Molecular Biology, University of South Alabama, Mobile, AL 36688; and [k]Department of Pediatrics, Boston Children's Hospital, Harvard Medical School, Boston, MA 02215

1. H. K. Arnold, R. C. Sears, A tumor suppressor role for PP2A-B56α through negative regulation of c-Myc and other key oncoproteins. *Cancer Metastasis Rev.* **27**, 147–158 (2008).
2. N. Wlodarchak, Y. Xing, PP2A as a master regulator of the cell cycle. *Crit. Rev. Biochem. Mol.* **51**, 162–184 (2016).
3. D. M. Virshup, Protein phosphatase 2A: A panoply of enzymes. *Curr. Opin. Cell Biol.* **12**, 180–185 (2000).
4. S. Strack *et al.*, Protein phosphatase 2A holoenzyme assembly: Identification of contacts between B-family regulatory and scaffolding A subunits. *J. Biol. Chem.* **277**, 20750–20755 (2002).
5. A. Saraf, E. A. Oberg, S. Strack, Molecular determinants for PP2A substrate specificity: Charged residues mediate dephosphorylation of tyrosine hydroxylase by the PP2A/B′ regulatory subunit. *Biochemistry* **49**, 986–995 (2010).
6. Y. Shi, Serine/threonine phosphatases: Mechanism through structure. *Cell* **139**, 468–484 (2009).
7. D. D. D. Study, Prevalence and architecture of de novo mutations in developmental disorders. *Nature* **542**, 433–438 (2017).
8. L. Shang *et al.*, De novo missense variants in PPP2R5D are associated with intellectual disability, macrocephaly, hypotonia, and autism. *Neurogenetics* **17**, 43–49 (2016).
9. G. Houge *et al.*, B56delta-related protein phosphatase 2A dysfunction identified in patients with intellectual disability. *J. Clin. Invest.* **125**, 3051–3062 (2015).
10. E. Cerami *et al.*, The cBio cancer genomics portal: An open platform for exploring multidimensional cancer genomics data. *Cancer Discov.* **2**, 401–404 (2012).
11. J. Gao *et al.*, Integrative analysis of complex cancer genomics and clinical profiles using the cBioPortal. *Sci. Signal.* **6**, pl1 (2013).
12. D. Biswas, W. Cary, J. A. Nolta, PPP2R5D-related intellectual disability and neurodevelopmental delay: A review of the current understanding of the genetics and biochemical basis of the disorder. *Int. J. Mol. Sci.* **21**, 1286 (2020).
13. N. Oyama *et al.*, Clinical, neuroimaging and molecular characteristics of PPP2R5D-related neurodevelopmental disorders: An expanded series with functional characterisation and genotype-phenotype analysis. *J. Med. Genet.* **60**, 511–522 (2022).
14. I. M. Walker *et al.*, PPP2R5D genetic mutations and early-onset parkinsonism. *Ann. Neurol.* **89**, 194–195 (2021).
15. K. Hetzelt *et al.*, Early-onset parkinsonism in PPP2R5D-related neurodevelopmental disorder. *Eur. J. Med. Genet.* **64**, 104123 (2021).
16. C. Y. Kim *et al.*, Early-onset parkinsonism is a manifestation of the PPP2R5D p. E200K mutation. *Ann. Neurol.* **88**, 1028–1033 (2020).
17. C. G. Wu *et al.*, PP2A-B′ holoenzyme substrate recognition, regulation and role in cytokinesis. *Cell Discov.* **3**, 17027 (2017).
18. E. P. Hertz *et al.*, A conserved motif provides binding specificity to the PP2A-B56 phosphatase. *Mol. Cell* **63**, 686–695 (2016).
19. J. Wang *et al.*, Crystal structure of a PP2A B56-BubR1 complex and its implications for PP2A substrate recruitment and localization. *Protein Cell* **7**, 516–526 (2016).
20. N. E. Davey, D. O. Morgan, Building a regulatory network with short linear sequence motifs: Lessons from the degrons of the anaphase-promoting complex. *Mol. Cell* **64**, 12–23 (2016).
21. N. E. Davey, M. S. Cyert, A. M. Moses, Short linear motifs–ex nihilo evolution of protein regulation. *Cell Commun. Signal.* **13**, 43 (2015).
22. C. P. Wigington *et al.*, Systematic discovery of Short Linear Motifs decodes calcineurin phosphatase signaling. *Mol. Cell* **79**, 342–358.e12 (2020).
23. Y. Ueki *et al.* A consensus binding motif for the PP4 protein phosphatase. *Mol. Cell* **76**, 953–964.e6 (2019).
24. E. Heroes *et al.*, The PP1 binding code: A molecular-lego strategy that governs specificity. *FEBS J.* **280**, 584–595 (2013).
25. I. Nasa, S. F. Rusin, A. N. Kettenbach, G. B. Moorhead, Aurora B opposes PP1 function in mitosis by phosphorylating the conserved PP1-binding RVxF motif in PP1 regulatory proteins. *Science Signal.* **11**, eaai8669 (2018).
26. X. Wang, R. Bajaj, M. Bollen, W. Peti, R. Page, Expanding the PP2A interactome by defining a B56-specific SLiM. *Structure* **24**, 2174–2181 (2016).
27. T. Kruse *et al.*, Direct binding between BubR1 and B56-PP2A phosphatase complexes regulate mitotic progression. *J. Cell Sci.* **126**, 1086–1092 (2013).
28. R. N. Bastos, M. J. Cundell, F. A. Barr, KIF4A and PP2A-B56 form a spatially restricted feedback loop opposing Aurora B at the anaphase central spindle. *J. Cell Biol.* **207**, 683–693 (2014).
29. Y. Ueki *et al.*, A highly conserved pocket on PP2A-B56 is required for hSgo1 binding and cohesion protection during mitosis. *Embo Rep.* **22**, e52295 (2021).
30. A. Ito *et al.*, A truncated isoform of the PP2A B56 subunit promotes cell motility through paxillin phosphorylation. *Embo J.* **19**, 562–571 (2000).
31. Y. Li *et al.*, Coupling to short linear motifs creates versatile PME-1 activities in PP2A holoenzyme demethylation and inhibition. *Elife* **11**, e79736 (2022).
32. S. M. Ambjorn *et al.*, A complex of BRCA2 and PP2A-B56 is required for DNA repair by homologous recombination. *Nat. Commun.* **12**, 5748 (2021).
33. S. H. Kim, C. G. Wu, W. Jia, Y. Xing, R. S. Tibbetts, Roles of constitutive and signal-dependent protein phosphatase 2A docking motifs in burst attenuation of the cyclic AMP response element-binding protein. *J. Biol. Chem.* **297**, 100908 (2021).
34. C. Lambrecht *et al.*, Loss of protein phosphatase 2A regulatory subunit B56delta promotes spontaneous tumorigenesis in vivo. *Oncogene* **37**, 544–552 (2018).
35. L. Liu, R. N. Eisenman, Regulation of c-Myc protein abundance by a protein phosphatase 2A-gGlycogen synthase kinase 3beta-negative feedback pathway. *Genes. Cancer* **3**, 23–36 (2012).
36. H. K. Arnold *et al.*, The Axin1 scaffold protein promotes formation of a degradation complex for c-Myc. *Embo J.* **28**, 500–512 (2009).
37. H. K. Arnold, R. C. Sears, A tumor suppressor role for PP2A-B56alpha through negative regulation of c-Myc and other key oncoproteins. *Cancer Metast. Rev.* **27**, 147–158 (2008).
38. H. K. Arnold, R. C. Sears, Protein phosphatase 2A regulatory subunit B56alpha associates with c-myc and negatively regulates c-myc accumulation. *Mol Cell Biol.* **26**, 2832–2844 (2006).
39. K. L. Dodge-Kafka *et al.*, cAMP-stimulated protein phosphatase 2A activity associated with muscle A kinase-anchoring protein (mAKAP) signaling complexes inhibits the phosphorylation and activity of the cAMP-specific phosphodiesterase PDE4D3. *J. Biol. Chem.* **285**, 11078–11086 (2010).
40. J. H. Ahn *et al.*, Protein kinase A activates protein phosphatase 2A by phosphorylation of the B56delta subunit. *Proc. Natl. Acad. Sci. U.S.A.* **104**, 2979–2984 (2007).
41. M. P. Flynn *et al.*, Luteinizing hormone receptor activation in ovarian granulosa cells promotes protein kinase A-dependent dephosphorylation of microtubule-associated protein 2D. *Mol. Endocrinol.* **22**, 1695–1710 (2008).
42. S. S. Margolis *et al.*, Role for the PP2A/B56delta phosphatase in regulating 14-3-3 release from Cdc25 to control mitosis. *Cell* **127**, 759–773 (2006).
43. C. M. Forester, J. Maddox, J. V. Louis, J. Goris, D. M. Virshup, Control of mitotic exit by PP2A regulation of Cdc25C and Cdk1. *Proc. Natl. Acad. Sci. U.S.A.* **104**, 19867–19872 (2007).
44. G. P. Shouse, Y. Nobumori, M. J. Panowicz, X. Liu, ATM-mediated phosphorylation activates the tumor-suppressive function of B56gamma-PP2A. *Oncogene* **30**, 3755–3765 (2011).
45. T. S. Levitz, E. J. Brignole, I. Fong, M. C. Darrow, C. L. Drennan, Effects of chameleon dispense-to-plunge speed on particle concentration, complex formation, and final resolution: A case study using the Neisseria gonorrhoeae ribonucleotide reductase inactive complex. *J. Struct. Biol.* **214**, 107825 (2022).
46. T. Jain, P. Sheehan, J. Crum, B. Carragher, C. S. Potter, Spotiton: A prototype for an integrated inkjet dispense and vitrification system for cryo-TEM. *J. Struct. Biol.* **179**, 68–75 (2012).
47. Y. Xu *et al.*, Structure of the protein phosphatase 2A holoenzyme. *Cell* **127**, 1239–1251 (2006).
48. U. S. Cho, W. Xu, Crystal structure of a protein phosphatase 2A heterotrimeric holoenzyme. *Nature* **445**, 53–57 (2007).
49. R. Appadurai, J. Nagesh, A. Srivastava, High resolution ensemble description of metamorphic and intrinsically disordered proteins using an efficient hybrid parallel tempering scheme. *Nat. Commun.* **12**, 958 (2021).
50. L. Wang, R. A. Friesner, B. J. Berne, Replica exchange with solute scaling: A more efficient version of replica exchange with solute tempering (REST2). *J. Phys. Chem. B* **115**, 9431–9438 (2011).
51. C. M. Papke *et al.*, A disorder-related variant (E420K) of a PP2A-regulatory subunit (PPP2R5D) causes constitutively active AKT-mTOR signaling and uncoordinated cell growth. *J. Biol. Chem.* **296**, 100313 (2021).
52. R. K. Dorer *et al.*, A small-molecule inhibitor of Mps1 blocks the spindle-checkpoint response to a lack of tension on mitotic chromosomes. *Curr. Biol.* **15**, 1070–1076 (2005).
53. S. Kadura, S. Sazer, SAC-ing mitotic errors: How the spindle assembly checkpoint (SAC) plays defense against chromosome mis-segregation. *Cell Motil. Cytoskelet.* **61**, 145–160 (2005).
54. R. Liu *et al.*, A novel nonsense mutation in PPP2R5D is associated with neurodevelopmental disorders and shows incomplete penetrance in a Chinese pedigree. *Clin. Neurol. Neurosur.* **223**, 107524 (2022).
55. K. A. Konovalov *et al.*, Disease mutations and phosphorylation alter the allosteric pathways involved in autoinhibition of protein phosphatase 2A. *J. Chem. Phys.* **158**, 215101 (2023).
56. V. Stanevich *et al.*, The structural basis for tight control of PP2A methylation and function by LCMT-1. *Mol Cell* **41**, 331–342 (2011).
57. L. Zhang *et al.*, Eya3 partners with PP2A to induce c-Myc stabilization and tumor progression. *Nat Commun.* **9**, 1047 (2018), 10.1038/s41467-018-03327-4.
58. H. Wei *et al.*, Optimizing "self-wicking" nanowire grids. *J. Struct. Biol.* **202**, 170–174 (2018).
59. C. Suloway *et al.*, Automated molecular microscopy: The new Leginon system. *J. Struct. Biol.* **151**, 41–60 (2005).
60. A. Punjani, J. L. Rubinstein, D. J. Fleet, M. A. Brubaker, cryoSPARC: Algorithms for rapid unsupervised cryo-EM structure determination. *Nat. Methods* **14**, 290–296 (2017).
61. A. Punjani, D. J. Fleet, 3D variability analysis: Resolving continuous flexibility and discrete heterogeneity from single particle cryo-EM. *J. Struct. Biol.* **213**, 107702 (2021).
62. E. F. Pettersen *et al.*, UCSF Chimera–a visualization system for exploratory research and analysis. *J. Comput. Chem.* **25**, 1605–1612 (2004).
63. P. Emsley, B. Lohkamp, W. G. Scott, K. Cowtan, Features and development of Coot. *Acta Crystallogr. D Biol. Crystallogr.* **66**, 486–501 (2010).
64. P. D. Adams *et al.*, PHENIX: A comprehensive Python-based system for macromolecular structure solution. *Acta Crystallogr. D Biol. Crystallogr.* **66**, 213–221 (2010).
65. V. B. Chen *et al.*, MolProbity: All-atom structure validation for macromolecular crystallography. *Acta Crystallogr. D Biol. Crystallogr.* **66**, 12–21 (2010).
66. B. Hess, C. Kutzner, D. van der Spoel, E. Lindahl, Gromacs 4: Algorithms for highly efficient, load-balanced, and scalable molecular simulation. *J. Chem. Theory Comput.* **4**, 435–447 (2008).
67. J. A. Maier *et al.*, ff14SB: Improving the accuracy of protein side chain and backbone parameters from ff99SB. *J. Chem. Theory Comput.* **11**, 3696–3713 (2015).
68. J. B. Hopkins, R. E. Gillilan, S. Skou, BioXTAS RAW: Improvements to a free open-source program for small-angle X-ray scattering data reduction and analysis. *J. Appl. Crystallogr.* **50**, 1545–1553 (2017).
69. C. J. Jong *et al.*, Reduction of protein phosphatase 2A (PP2A) complexity reveals cellular functions and dephosphorylation motifs of the PP2A/B′δ holoenzyme. *J. Biol. Chem.* **295**, 5654–5668 (2020).
70. C. Wu *et al.*, The structure of the PP2A-B56Delta holoenzyme mutant - E197K. Electron Microscopy Data Bank. https://www.ebi.ac.uk/emdb/EMD-42018. Deposited 18 September 2023.
71. C. Wu *et al.*, The structure of the PP2A-B56Delta holoenzyme mutant - E197K. Electron Microscopy Data Bank. https://www.rcsb.org/structure/41837. Deposited 5 September 2023.
72. C. Wu *et al.*, The structure of the PP2A-B56Delta holoenzyme mutant - E197K. Protein Data Bank. https://www.rcsb.org/structure/8U89. Deposited 18 September 2023.
73. C. Wu *et al.*, The structure of the PP2A-B56Delta holoenzyme mutant - E197K. Protein Data Bank. https://www.rcsb.org/structure/8U1X. Deposited 5 September 2023.
74. Z. Xu., Protein phosphatase 2A (PP2A)-B56δ holoenzyme wildtype. Small Angle Scattering Biological Data Bank. https://www.sasbdb.org/data/SASDTW2. Deposited 30 October 2023.
75. Z. Xu., Protein phosphatase 2A (PP2A)-B56δ holoenzyme E198K mutant. Small Angle Scattering Biological Data Bank. https://www.sasbdb.org/data/SASDTX2. Deposited 30 October 2023.